Article

Mechanical Interlocking of 144 Symmetrical ^{19}F and Tetraphenylethylene for Magnetic Resonance-Fluorescence Dual Imaging

Lan Yang,[⊥] Fang Wang,[⊥] Yu Li,[⊥] Rui Zhou, Anfeng Li, Tingjuan Wu, Maosong Qiu, Lei Zhang, Minghui Yang, Xin Zhou, Zhong-Xing Jiang,* and Shizhen Chen*
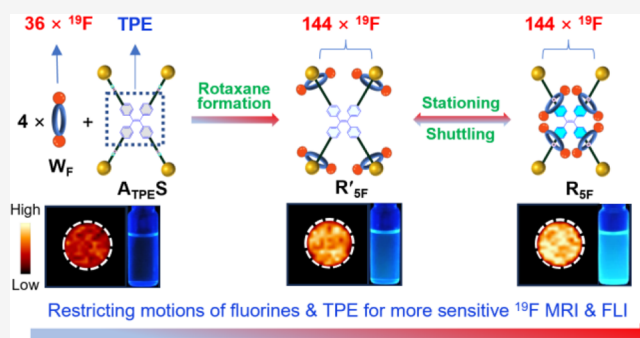
ACCESS | Metrics & More | Article Recommendations | SI Supporting Information

ABSTRACT: Single-molecule dual ^{19}F magnetic resonance imaging (^{19}F MRI) and fluorescence imaging (FLI) agents are valuable tools in biomedical research. However, integrating millimolar-sensitivity ^{19}F MRI and micromolar-sensitivity FLI into a single molecule remains challenging. Here, we report the use of mechanically interlocked [5]rotaxanes to efficiently incorporate 144 symmetrical fluorines (^{19}F) for sensitive ^{19}F MRI and to control the motion of tetraphenylethylene (TPE) for responsive FLI at the molecular level, yielding a dual imaging agent with micromolar sensitivity. The sensitivity gap between ^{19}F MRI and FLI is bridged by generating an intense singlet ^{19}F peak from 144 symmetrical ^{19}F and modulating their motion through mechanical interlocking. Spectroscopic and imaging studies, in conjunction

with molecular dynamics simulations, highlight the critical role of [5]rotaxane formation, wheel "stationing-shuttling", and the introduction of fluorous bulky perfluoro-*tert*-butoxymethyl (PFBM) groups as effective strategies to improve ^{19}F MRI sensitivity and enable responsive FLI. This work not only advances the development of high-performance dual imaging agents but also provides valuable insights into the structure, dynamics, and potential applications of [5]rotaxanes in materials science.

INTRODUCTION

Single-molecule dual ^{19}F magnetic resonance imaging (^{19}F MRI) and fluorescence imaging (FLI) agents are invaluable tools in biomedical research,[1−8] providing complementary capabilities. FLI offers sensitive visualization of cells and superficial tissues,[3,6] while ^{19}F MRI enables quantitative "hot spot" imaging of deep tissues.[7] In addition, the single-molecule agents not only simplify the imaging process but also allow for high spatial precision and colocalization. However, the development of such dual imaging agents has been hindered by the significant disparity in sensitivity levels: ^{19}F MRI typically requires millimolar concentrations for detection,[9] while FLI operates at micromolar concentrations.[10,11] Strategies such as integrating multiple chemically equivalent ^{19}F[12−18] or optimizing longitudinal relaxation time (T_1)[19,20] have been explored to enhance ^{19}F MRI sensitivity and bridge the sensitivity gap between the two modalities. However, to the best of our knowledge, no ^{19}F MRI−FLI dual imaging agent has successfully operated at micromolar concentrations.

The performance of imaging agents is strongly influenced by their motion state, which affects both sensitivity and responsiveness. For example, tetraphenylethylene (TPE) fluorophores exhibit minimal fluorescence in a freely moving state but become highly emissive when motion is

restricted,[21,22] a phenomenon known as aggregation-induced emission (AIE). This motion-dependent behavior is crucial for developing stimulus-responsive FLI agents.[23−25] In the case of ^{19}F MRI agents, the mobility of ^{19}F directly influences their magnetic relaxation, which is critical for achieving high sensitivity in MRI. Modulating the motion of ^{19}F to shorten their T_1 while preserving an adequate transverse relaxation time (T_2) is an effective strategy for enhancing MRI sensitivity.[26−28] However, controlling motion in imaging agents remains a significant challenge. For instance, while aggregation can induce AIE in fluorophores, it often leads to aggregation-caused quenching (ACQ),[23,24,29] and the aggregation of ^{19}F MRI agents tends to decrease signal intensity.[30] Addressing these challenges requires innovative strategies to control motion effectively.
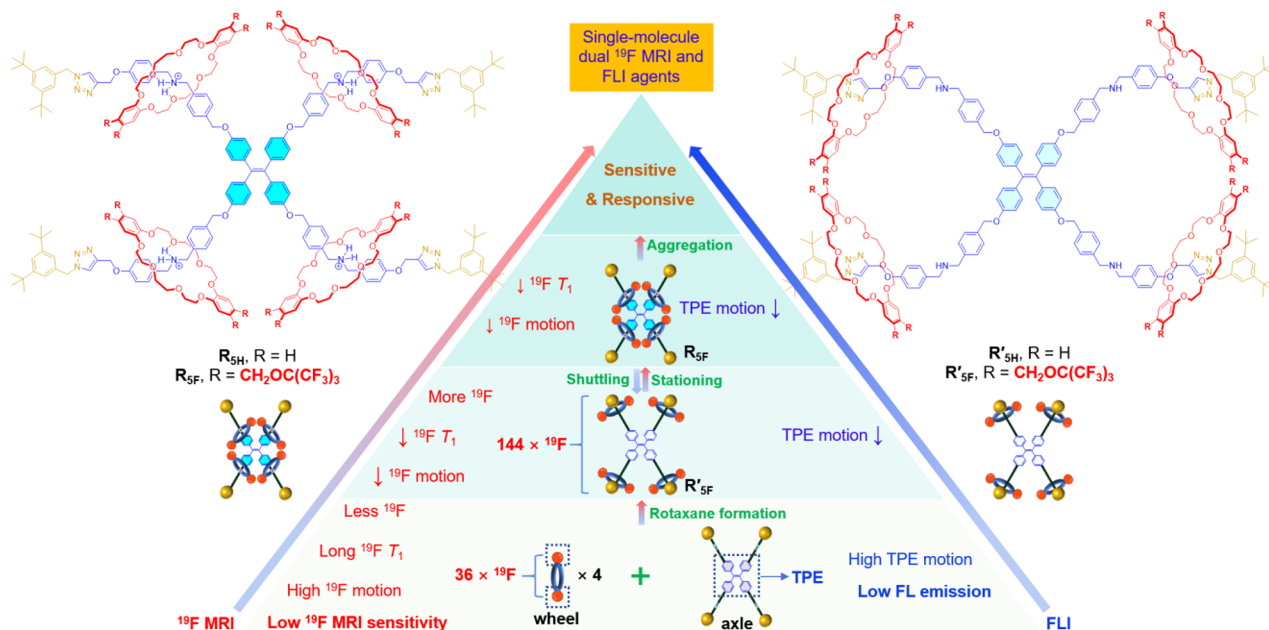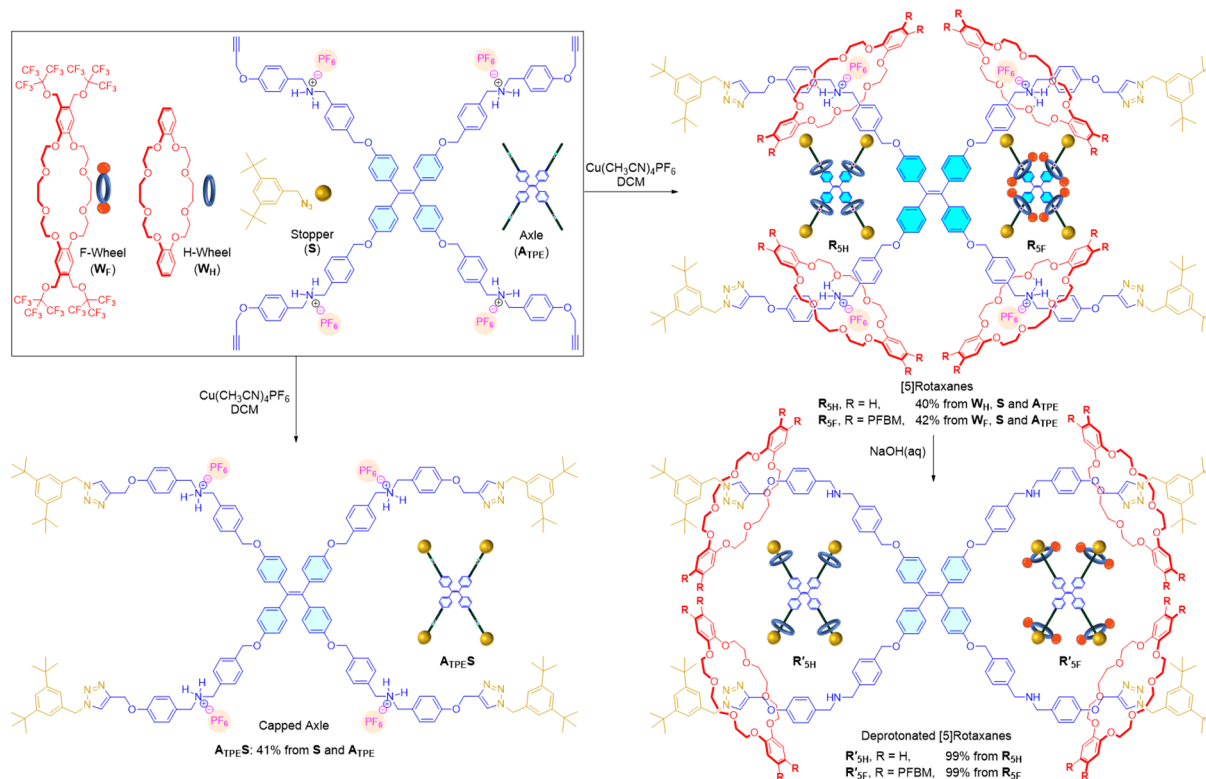
Figure 1. Development of fluorinated TPE [5]rotaxanes as sensitive and responsive dual ^{19}F MRI−FLI agents by integrating 144 chemically equivalent ^{19}F and a TPE fluorophore and restricting their motions.

Scheme 1. Synthesis of [5]Rotaxanes R_{5H}, R_{5F}, R'_{5H}, R'_{5F}, and Capped Axle $A_{TPE}S^a$

^{a}The preparation of wheel W_F, stopper S, and axle A_{TPE} is described in the Supporting Information.

Rotaxanes, mechanically interlocked molecules consisting of cyclic wheels threaded onto axles and capped by bulky stoppers,[31−37] provide a promising approach for motion control. The formation of rotaxanes restricts the motion of their components through mechanical interlocking, while the responsive "stationing-shuttling" motion of the wheel enables precise manipulation of both wheel and axle dynamics. For

example, the fluorinated [2]rotaxane **Rx-2** demonstrates how restricting the motion of ^{19}F on the wheel can significantly shorten T_1 and improve the T_2/T_1 ratio.[38] In ^{19}F MRI, a short T_1 enhances the signal acquisition speed,[19,20] while a high T_2/T_1 ratio reduces signal loss,[26−28] thereby improving sensitivity. **Rx-2** has shown a 79% improvement in sensitivity compared to its wheel molecule, illustrating the power of rotaxanes for
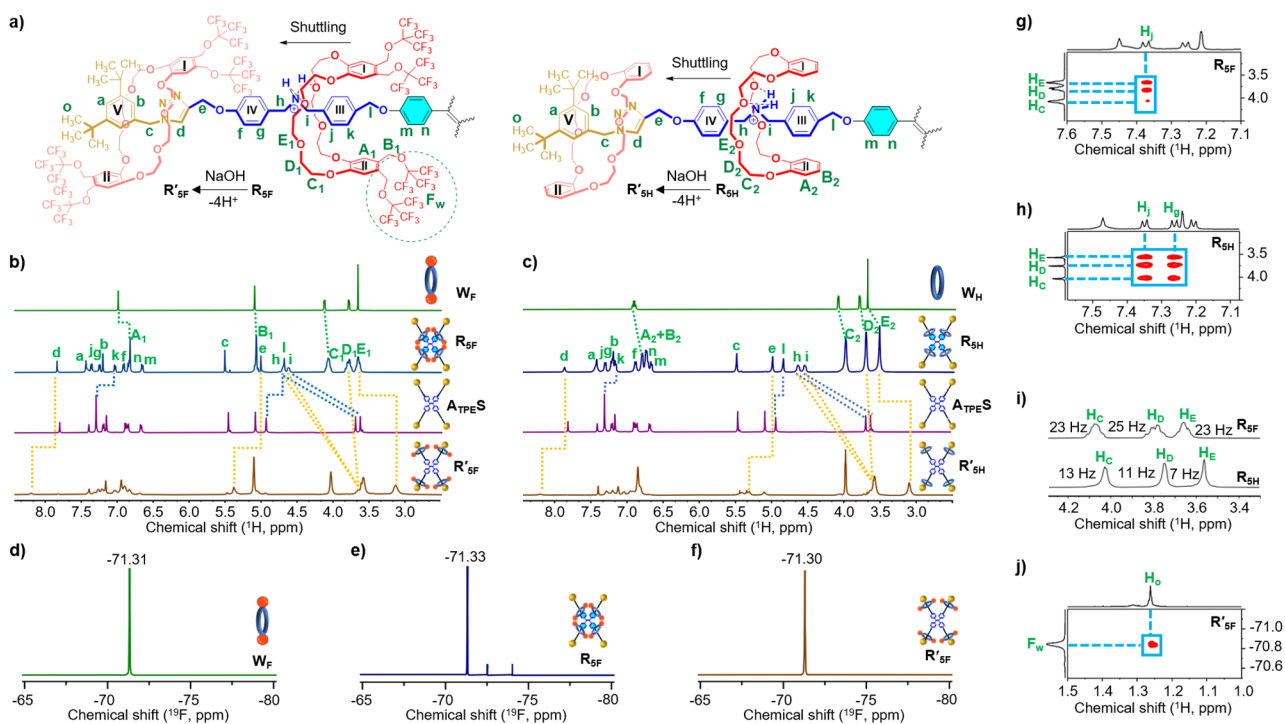
Figure 2. Proposed stable conformations of the [5]rotaxanes (a, illustrated by one of their branches with labeled protons). Partial ^{1}H NMR spectra of W_F, R_{5F}, $A_{TPE}S$, and R'_{5F} (b) and W_H, R_{5H}, $A_{TPE}S$, and R'_{5H} (c). ^{19}F NMR spectra of W_F (d), R_{5F} (e), and R'_{5F} (f). Partial ^{1}H$-^1$H ROESY NMR spectra of R_{5F} (g) and R_{5H} (h). Expanded ^{1}H NMR spectra of H_C-H_E regions with the indicated half-peak width of R_{5F} and R_{5H} (i). ^{1}H$-^{19}$F HOESY NMR spectrum of R'_{5F} (j). NMR conditions: 2.5 mM in CD$_3$CN at 298 K, 500 MHz for 1D NMR, and 600 MHz for 2D NMR.

controlling motion and enhancing imaging performance.[38] The integration of ^{19}F MRI and FLI agents into rotaxanes—leveraging their ability to incorporate large numbers of chemically equivalent ^{19}F for sensitive ^{19}F MRI sensitivity and modulate the motion of the fluorophore for responsive FLI—holds promise for overcoming current challenges and delivering high-performance dual imaging agents.

Here, as a proof of concept, we demonstrate the use of [5]rotaxanes to integrate four fluorinated wheels and a TPE fluorophore with motion control to enhance sensitivity and enable stimulus responsiveness. The resulting fluorinated TPE [5]rotaxane, R_{5F}, serves as a sensitive and responsive dual ^{19}F MRI–FLI agent (Figure 1). In R_{5F}, 16 perfluoro-*tert*-butoxymethyl (PFBM) groups are symmetrically placed on the benzene rings of the dibenzo-24-crown-8 wheels to optimize ^{19}F MRI sensitivity, while a TPE fluorophore is positioned at the core of the tetragonal axle to enable FLI. This mechanically interlocked structure integrates 144 chemically equivalent ^{19}F, generating an intense singlet ^{19}F NMR peak, which enables sensitive ^{19}F MRI with concentrations comparable to those used for FLI. Although many ^{19}F MRI agents have 27 or 36 equivalent ^{19}F with even higher fluorine content, R_{5F}'s 144 equivalent ^{19}F significantly reduces the detectable molecular concentration.[16,39−42] Furthermore, "wheel-stationing" in R_{5F} restricts TPE motion, thereby enhancing fluorescence emission. In contrast, "wheel-shuttling" in R'_{5F} partially relaxes these restrictions, leading to reduced fluorescence emission. By exploiting the acid/base-responsive "stationing-shuttling" behavior of the wheels, TPE motions can be controlled, enabling stimulus-responsive FLI with "dim-bright" contrast. This strategy allows R_{5F} to achieve micro-molar ^{19}F MRI sensitivity, effectively bridging the sensitivity gap with FLI, and enables the stimulus-responsive manipu-

lation of FLI at the single-molecule level. Nonfluorinated [5]rotaxanes, R_{5H} and R'_{5H}, were designed as controls to investigate the influence of the PFBM groups on sensitivity and functionality. This study also provides insights into the structure, dynamics, motion, and aggregation behavior of [5]rotaxanes.

■ RESULTS AND DISCUSSION

With the design in mind, [5]rotaxanes R_{5H} and R_{5F} were synthesized using a one-pot thread-and-cap strategy based on the "click reaction" (Scheme 1).[38] Despite multiple reaction centers and components, the assembly of wheels W_H/W_F, axle A_{TPE}, and stopper S into R_{5H} and R_{5F} was efficiently achieved. Subsequent treatment of R_{5H} and R_{5F} with sodium hydroxide afforded deprotonated [5]rotaxanes R'_{5H} and R'_{5F} in high yields. Capped axle $A_{TPE}S$ with a conventional AIE structure was also prepared as a control. The formation of [5]rotaxanes was confirmed by ^{1}H/^{13}C/^{19}F NMR spectroscopy and mass spectrometry (see the Supporting Information).

To evaluate the structure and intramolecular motion of R_{5F}, the wheel−axle interactions were investigated. Compared to $A_{TPE}S$, significant downfield shifts of axle protons H_h and H_i in the ^{1}H NMR spectra of R_{5F} and R_{5H} indicated hydrogen bonding-induced "wheel-stationing" around the positively charged amines (Figures 2a−c and S1). Additionally, upfield shifts of protons H_A-H_C, H_k, and H_l in R_{5F} (Figures 2b and S1a) and H_A-H_E, H_k, and H_l in R_{5H} (Figures 2c and S1b) relative to W_F/W_H and $A_{TPE}S$ indicated the presence of $\pi-\pi$ interactions between axle phenyl groups III and wheel phenyl groups I and II.[43−45] As designed, 144 ^{19}F in R_{5F} and R'_{5F} collectively produced an intense singlet ^{19}F NMR peak (Figure 2d−f). Further ^{1}H$-^1$H ROESY NMR analysis revealed one set of cross-peaks between wheel protons H_C-H_E and axle

pubs.acs.org/JACS

protons H_j in R_{5F} (Figures 2g and S2a) and two sets of cross-peaks with axle protons H_j and H_g in R_{5H} (Figures 2h and S2b), highlighting that the fluorinated wheels in R_{5F} are more centrally oriented to the TPE core compared to R_{5H}. Finally, the significantly broader and split ^1H peaks of wheel protons $H_C–H_E$ in R_{5F} compared to those in R_{5H} (Figure 2i) suggested multiple motion-restricted conformations of the fluorinated wheels. These observations suggested that, probably driven by the fluorous effect[46,47] of the 16 PFBM groups, the fluorinated wheels in R_{5F} accumulated rigidly around the TPE to form a fluorous "donut ring" with significantly restricted wheel ^{19}F and TPE motions.

The wheel−axle interactions in R'_{5H} and R'_{5F} were also investigated. Compared with R_{5H} and R_{5F}, upfield shifts of axle protons H_h and H_i in the ^1H NMR spectra of R'_{5H} and R'_{5F} indicated the absence of hydrogen bonding, while downfield shifts of axle protons H_d and H_e suggested $\pi−\pi$ interactions between wheel phenyl group I and axle triazole (Figure 2a–c).[48,49] The $^1H–^{19}F$ HOESY NMR spectrum of R'_{5F} displayed cross-peaks between wheel ^{19}F (F_W) and axle protons H_o and H_e, indicating their adjacency and an "S-shaped" conformation of the wheels (Figures 2j and S3). The absence of hydrogen bonding allowed for multiple stable conformations, as evidenced by broad and split ^1H peaks (Figures 2b,c and S1).[50] Thus, "wheel-shuttling" in R'_{5F} released wheel ^{19}F from the restriction of fluorous effect and hydrogen bonding.

Since the motion of spin nuclei can be assessed by relaxation times, with the less motion, the shorter relaxation times, the relaxation times of characteristic fluorines and protons in the [5]rotaxanes and their precursors were compared. For wheel fluorines F_W, the assembly of W_F into R_{5F} significantly shortened the relaxation times ($\Delta T_1 = -31\%$, $\Delta T_2 = -46\%$), while the transformation of R_{5F} into R'_{5F} caused small increases ($\Delta T_1 = 4.7\%$, $\Delta T_2 = 5.1\%$), indicating that [5]rotaxane formation rather than wheel positioning dominated wheel ^{19}F motion (Figures 3a, S4, S5 and Table S1). For axle *tert*-butyl H_o, R_{5F} showed slight decreases in relaxation times compared to $A_{TPE}S$ ($\Delta T_1 = -5.2\%$, $\Delta T_2 = -0.2\%$), while R'_{5F} showed more decreases ($\Delta T_1 = -14.6\%$, $\Delta T_2 = -11.5\%$), indicating a more dramatic restriction of stopper motion by adjacent wheels (Figures 3b, S4, S5 and Table S2). The same trends were observed for R_{5H} and R'_{5H}. For TPE H_m, R_{5F} showed significant decreases in relaxation times compared to $A_{TPE}S$ ($\Delta T_1 = -14.5\%$, $\Delta T_2 = -51.0\%$), in contrast to much smaller changes for R_{5H} ($\Delta T_1 = 19.8\%$, $\Delta T_2 = -20.1\%$), reflecting a more efficient restriction of TPE motion by fluorinated wheels (Figures 3c, S4, S5 and Table S3). Interestingly, the temperature-dependent relaxation study of R_{5F} and R'_{5F} showed a good proportional relationship, highlighting the potential of [5]rotaxanes as valuable temperature probes (Figure 3d). Therefore, the incorporation of W_F into R_{5F} significantly restricted the motion of wheel ^{19}F and TPE for more sensitive ^{19}F MRI and FLI.

As designed, R_{5F} exhibited a 45% higher T_1-weighted ^{19}F MRI signal intensity (SI) compared to 4 equiv of W_F (Figure 3e). In terms of molecular sensitivity, 5.8 equiv of W_F were required to produce the same SI as R_{5F}, a considerable improvement in ^{19}F MRI sensitivity. With 144 symmetrical ^{19}F, a short T_1, and a high T_2/T_1 ratio of 0.68, R_{5F} was imaged at a low concentration of 16 μM ($C_F = 2.3$ mM) with a short data acquisition time of 307 s and a signal-to-noise ratio (SNR) of 3.2 (Figure 3e). Since R_{5F} was detected by ^{19}F MRI in the same concentration range as regular FLI agents, the
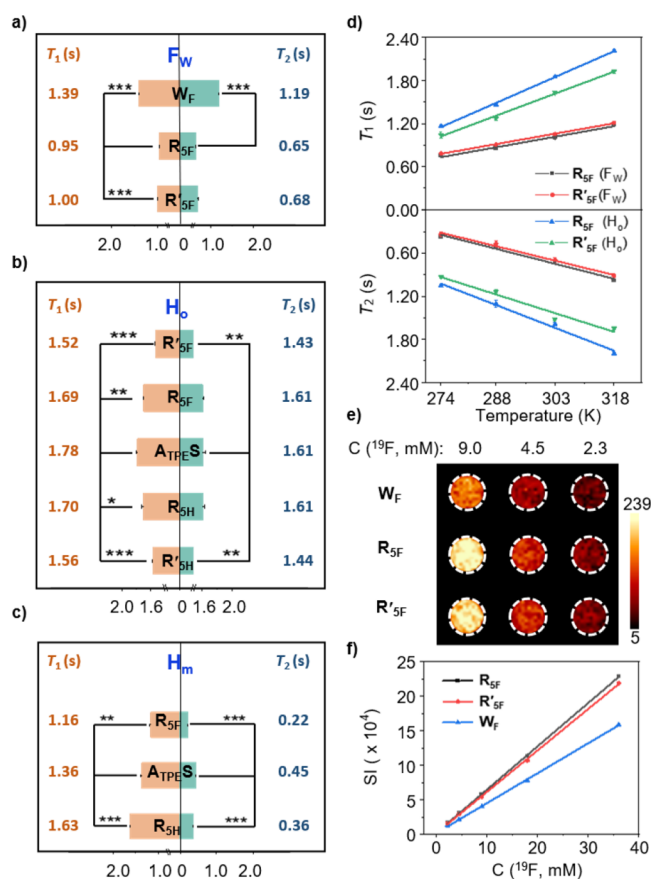

Figure 3. Relaxation times of wheel fluorines F_W in W_F, R_{5F}, and R'_{5F} (a), axle *tert*-butyl protons H_o in R'_{5F}, R_{5F}, $A_{TPE}S$, R_{5H}, and R'_{5H} (b), and TPE protons H_m in R_{5F}, $A_{TPE}S$, and R_{5H} (c). Temperature-dependent relaxation times of F_W and H_o in R_{5F} and R'_{5F} (d). ^{19}F MRI phantom images (e, 9.4 T, 298 K, CH$_3$CN) and the plot of signal intensity versus concentration (^{19}F) (f) of R_{5F}, R'_{5F}, and W_F. Statistical significance: $*p < 0.05$, $**p < 0.01$, and $***p < 0.001$. NMR conditions: 500 MHz (a, b, and d) or 600 MHz (c), 298 K, and 1.0 mM in CD$_3$CN.

sensitivity gap between ^{19}F MRI and FLI was bridged by the [5]rotaxane scaffold.[15−18] In contrast, R'_{5F} exhibited a slightly longer T_1, resulting in an up to 5.7% lower SI compared to R_{5F}. For W_F, R'_{5F}, and R_{5F}, the SI exhibited a proportional relationship to the ^{19}F concentration (Figure 3f), facilitating accurate quantification. Furthermore, the slope of the SI increase with concentration was greatest for R_{5F}, and thus, the differences in SI were more pronounced at higher concentrations. This is likely due to further restriction of fluorine motion under high-concentration conditions.

Having established their role in enhancing ^{19}F MRI sensitivity, we investigated the influence of motion restriction on the optical properties of the [5]rotaxanes. First, the [5]rotaxanes exhibited significantly higher UV absorption and molar extinction coefficients (ε) compared to $A_{TPE}S$ (Figures 4a, S6, and S7). However, "wheel-stationing" in R_{5F} and R_{5H} caused slight blue shifts in the characteristic TPE absorption peaks compared to $A_{TPE}S$ (Figures 4a and S6), while "wheel-shuttling" in R'_{5F} and R'_{5H} resulted in red-shifted TPE peaks, indicating that "wheel-stationing" weakened electronic interactions in the TPE by altering its conformation. Second, the [5]rotaxanes displayed red-shifted and enhanced FL emission compared to $A_{TPE}S$ (Figure 4b), with R_{5F} exhibiting the most
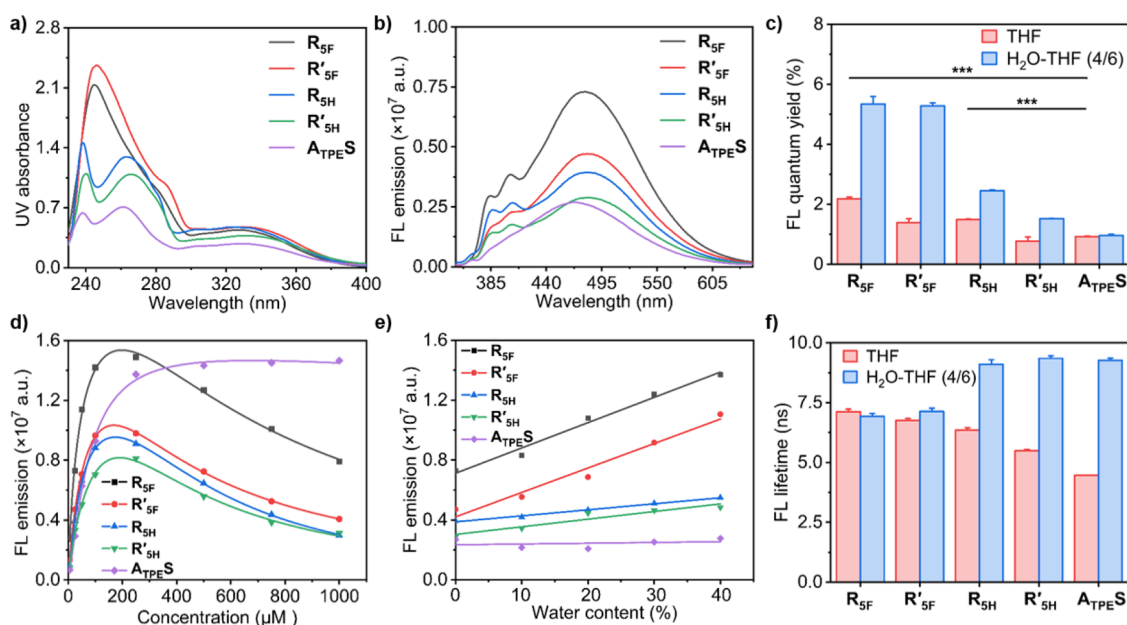
D

Figure 4. UV absorption spectra (a), FL emission spectra (b), FL quantum yield (c), plots of maximum FL emission versus concentration (d) and water content (e), and FL lifetime (f) of R_{5F}, R'_{5F}, R_{5H}, R'_{5H}, and $A_{TPE}S$. Solvents: THF for (a), (b), and (d); H_2O-THF mixture for (c), (e), and (f). Statistical significance: *$p < 0.05$, **$p < 0.01$, and ***$p < 0.001$.
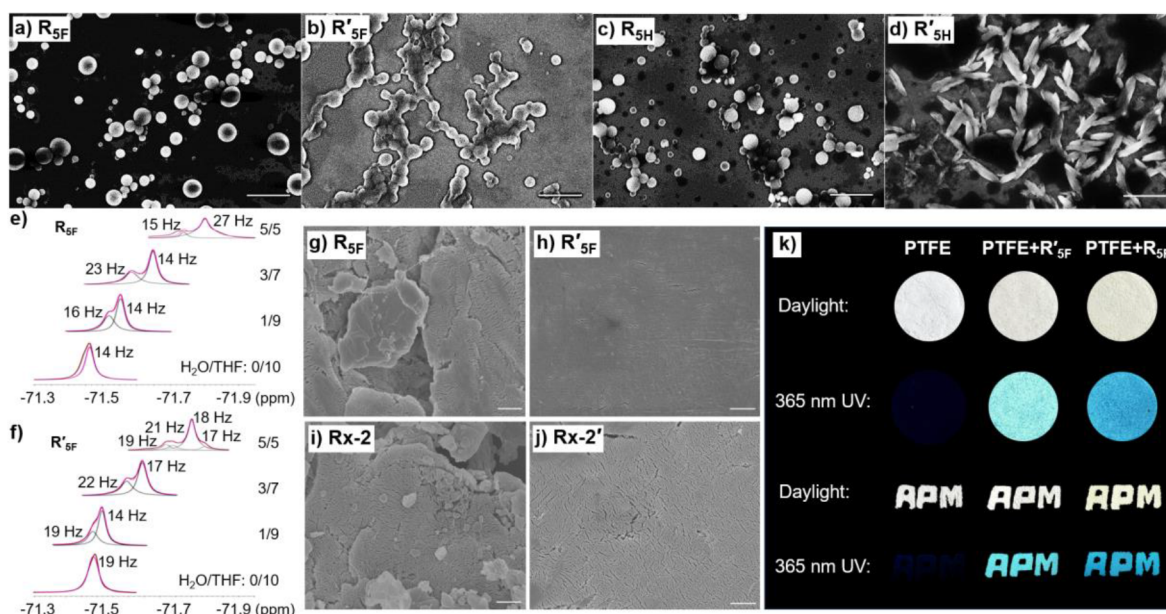

Figure 5. SEM images of R_{5F} (a), R'_{5F} (b), R_{5H} (c), and R'_{5H} (d) aggregated in H_2O-THF (4:6) on silicon chips. Partial solvent-dependent ^{19}F NMR spectra with fitted peaks of R_{5F} (e) and R'_{5F} (f). SEM images of R_{5F} (g), R'_{5F} (h), Rx-2 (i), and Rx-2' (j) aggregated in H_2O-THF (4:6) on PTFE microparticles. Photos of original and R'_{5F}- and R_{5F}-absorbed PTFE microparticles in 2 cm dishes and their sand paintings under daylight and a 365 nm UV lamp (k). Scale bars: 1 μm.

pronounced enhancement, 2.7 times higher than $A_{TPE}S$, suggesting restricted motion of TPE. Third, the absolute FL quantum yield (Φ_f) measurement showed that R_{5F} and R_{5H} exhibited 2.4-fold and 1.6-fold higher Φ_f in tetrahydrofuran (THF), respectively, compared to $A_{TPE}S$ (Figure 4c), underscoring the significant restriction of TPE motion due to "wheel-stationing". Thus, [5]rotaxane formation, especially the fluorinated ones, effectively restricts TPE motion to enhance FL emission and Φ_f, providing an effective monomolecular strategy to manipulate TPE FL, distinct from the multimolecular strategy in conventional TPE fluorophores.

We also investigated the effect of aggregation on the FL properties of the [5]rotaxanes. On the one hand, concentration-dependent FL studies revealed a significant decrease in FL emission above 150 μM for all [5]rotaxanes, in contrast to $A_{TPE}S$, which showed a typical AIE effect with stable FL up to 1000 μM (Figures 4d, S8, and S9). On the other hand, solvent-dependent FL studies showed greater water-induced enhancements of FL intensity and Φ_f in fluorinated [5]rotaxanes compared to nonfluorinated ones (Figures 4c,e and S10), while the trend was reversed for FL lifetime (Figures 4f and S11). These observations suggest that aggregation in THF is driven
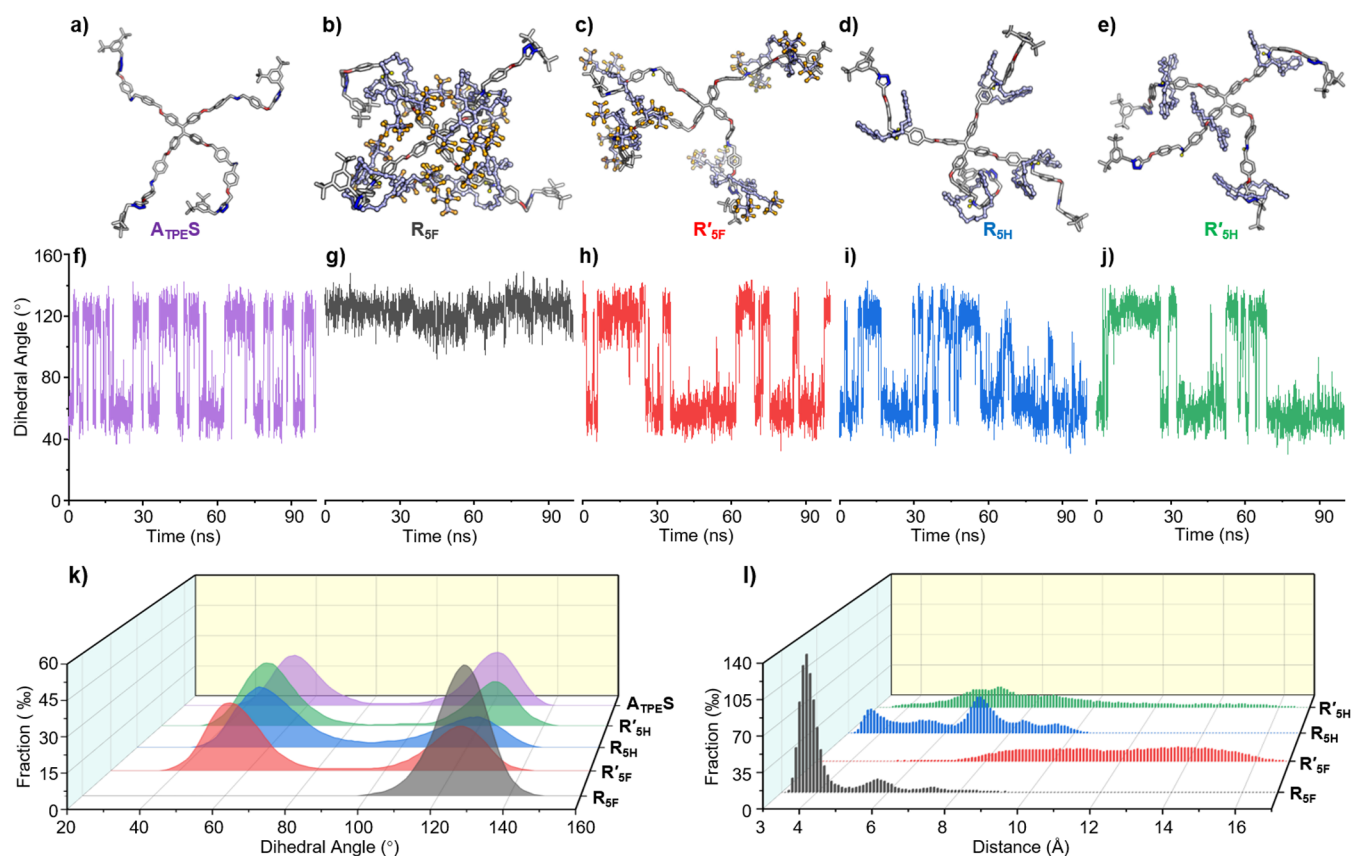
Figure 6. Simulated representative conformations of $A_{TPE}S$ (a), R_{5F} (b), R'_{5F} (c), R_{5H} (d), and R'_{5H} (e). Calculated dihedral angles between a phenyl group and the ethylene plane in the TPE of $A_{TPE}S$ (f), R_{5F} (g), R'_{5F} (h), R_{5H} (i), and R'_{5H} (j) and the plot of their fractions (k) over 100 ns. Calculated distance fractions between axle phenyl group III and wheel phenyl groups in the [5]rotaxanes (l). The corresponding simulated movies and the calculated distance can be found in the Supporting Information.

by intermolecular fluorous and $\pi-\pi$ interactions, which free the TPE from intramolecular interactions, increasing its motion and leading to reduced FL emission and shorter FL lifetimes. In contrast, water-induced aggregation is driven by hydrophilic−hydrophobic interactions to shield hydrophobic groups, especially the bulky highly hydrophobic PFBM groups, thereby restricting TPE motion for increased FL emission.[51] Additionally, a correlation between H_A and H_g was observed (Figure S12), likely due to the pronounced aggregation of hydrophobic groups.

The distinct solvent-dependent FL of [5]rotaxanes prompted us to investigate their aggregates by scanning electron microscopy (SEM) and ${}^{19}F$ NMR. SEM analysis revealed that R_{5F} and R_{5H} formed smooth spherical nanoparticles on silicon chips, whereas R'_{5F} formed highly adhesive spherical nanoparticles and R'_{5H} formed spindle-shaped nanoparticles (Figure 5a−d), demonstrating the significant influence of hydrogen bonding and PFBM groups on the aggregation behavior. Solvent-dependent ${}^{19}F$ NMR revealed a transition of most of the wheel ${}^{19}F$ in R_{5F} from a mobile state in THF to a restricted state in H_2O-THF (5:5), characterized by an almost doubled half-peak width (14 Hz versus 27 Hz, Figure 5e).[52,53] Conversely, the wheel ${}^{19}F$ in R'_{5F} remained mobile with similar half-peak widths (19 Hz versus 18 Hz, Figure 5f) as the water content was increased. The upfield shift of the ${}^{19}F$ peaks suggests that water induces a closer proximity between PFBM and phenyl groups to form a hydrophobic phase. These results underscore the influence of "wheel-stationing" and the fluorous effect in R_{5F}, resulting in more compact aggregates in the

presence of water with significantly restricted motion of wheel ${}^{19}F$.

In addition, polytetrafluoroethylene (PTFE) microparticles, a solid-phase fluorous extraction absorbent,[54] were employed to study the morphology and fluorous effect of the fluorinated rotaxane aggregates. In contrast to aggregation on silicon chips, SEM images showed that R_{5F} formed predominantly crystalline-like particles on the PTFE surface, while R'_{5F} infiltrated interstitial spaces and smoothed the PTFE surface (Figure 5g,h). Similar aggregation behaviors were observed with fluorinated [2]rotaxanes $Rx-2$ and $Rx-2'$ (Figure 5i,j),[38] highlighting that "wheel-shuttling" in R'_{5F} and $Rx-2'$ enhanced fluorous interactions with PTFE, likely due to their flexible morphology. Notably, fluorous absorption of R_{5F} and R'_{5F} resulted in brightly colored PTFE microparticles under a 365 nm UV lamp (Figure 5k), addressing the challenge of coloring PTFE materials. Interestingly, these microparticles have been utilized as fluorescent sands for sand painting, as shown in images from "APM", the acronym for this institute. The intriguing colors under UV light may find applications in counterfeiting.

To elucidate the molecular dynamics of the [5]rotaxanes, simulations were performed, and movies of their motions were generated (see the Supporting Information). Among them, R_{5F} showed the least motions in wheels and TPE. All four "C-shaped" wheels in R_{5F} "stationed" toward TPE without significant conformational transitions, while wheels in R_{5H} displayed rapid "C-shaped" inversions. Upon removal of
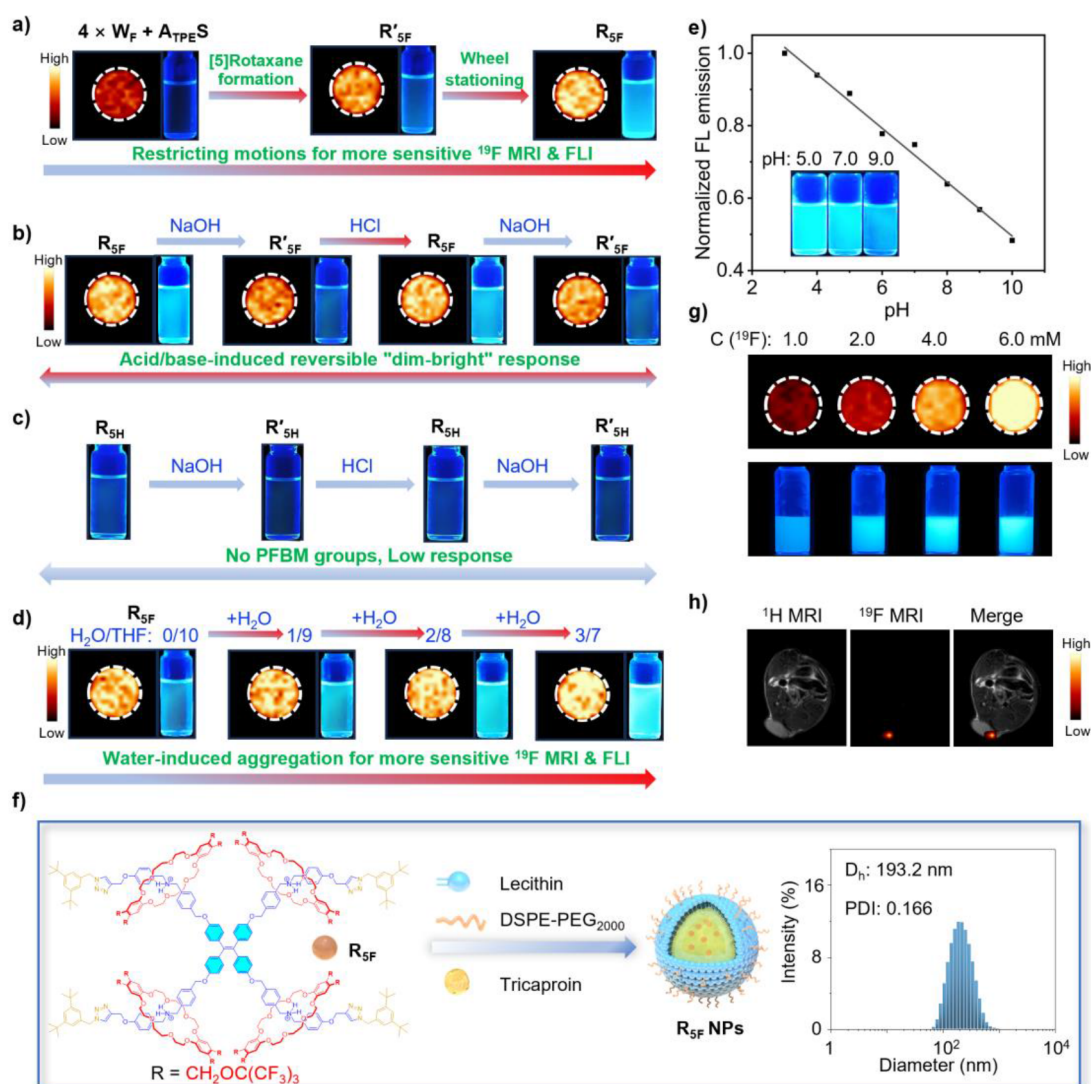
Figure 7. Responsive ^{19}F MRI (left circle) and FLI (right rectangle) showing the formation of $\mathbf{R'_{5F}}$ and "wheel-stationing" in $\mathbf{R_{5F}}$ (a), acid−base treatment of $\mathbf{R_{5F}}$ (b) and $\mathbf{R_{5H}}$ (c), water-induced aggregation of $\mathbf{R_{5F}}$ (d), and the linear relationship between maximum FL emission and pH in water-THF (3:7) solutions with inserted FLI photos at typical pH (e) for $\mathbf{R_{5F}}$. Schematic illustration and DLS analysis of nanoemulsion $\mathbf{R_{5F}NPs}$ (f), ^{19}F MRI (upper) and FLI (lower) of $\mathbf{R_{5F}NPs}$ at the indicated concentrations (g), and ^{1}H/^{19}F MRI of nude mice bearing U87-MG tumors after intratumoral injection of $\mathbf{R_{5F}NPs}$ (h). Concentration: 25 μM for $\mathbf{A_{TPE}S}$, $\mathbf{R_{5F}}$, $\mathbf{R'_{5F}}$, and $\mathbf{R_{5H}}$; 100 μM for $\mathbf{W_F}$. Solvents: THF for (a); chloroform for (b) and (c); water-THF for (d) and (e).

hydrogen bonding, all wheels in $\mathbf{R'_{5F}}$ "shuttled" to the triazoles and remained there, while wheels in $\mathbf{R'_{5H}}$ continued to "shuttle" between the triazoles and amines. Simulated snapshots (Figure 6a−e) show different conformations: $\mathbf{R_{5F}}$ shows a centrally oriented conformation, while $\mathbf{R_{5H}}$ shows divergent conformations. $\mathbf{R'_{5F}}$ shows a more uniform distribution of wheels at the triazoles than $\mathbf{R'_{5H}}$. These observations highlight the significant influence of steric hindrance and the fluorous effect of PFBM groups on the stable conformations and responsiveness of fluorinated [5]-rotaxanes. To show the influence of wheels on TPE motion, the dihedral angles between its phenyl groups and ethylene plane were calculated (Figures 6f−k and S13). $\mathbf{A_{TPE}S}$ showed an approximately even distribution around 55 and 122°. "Wheel-stationing" resulted in a dominant distribution around 127° in $\mathbf{R_{5F}}$ and a dispersed distribution around 58 and 122° in $\mathbf{R_{5H}}$, while "wheel-shuttling" resulted in distributions around 55 and 123° in $\mathbf{R'_{5F}}$. Finally, the distances between axle phenyl

groups III and wheel phenyl groups in [5]rotaxanes were evaluated (Figures 6l and S14−S17). $\mathbf{R_{5F}}$ exhibited the shortest distance (~3.7 Å, fraction up to 0.14), in contrast to $\mathbf{R_{5H}}$ which showed a wider distribution (3.7−9.4 Å). "Wheel-shuttling" in $\mathbf{R'_{5F}}$ and $\mathbf{R'_{5H}}$ significantly increased these distances, especially in $\mathbf{R'_{5F}}$ with bulky PFBM groups, suggesting strong $\pi-\pi$ interactions and fluorous effect in $\mathbf{R_{5F}}$. These simulations underscore the propensity of fluorinated wheels to restrict wheel ^{19}F and TPE motions, stabilize the centrally oriented conformation of $\mathbf{R_{5F}}$, and enhance FL emission and ^{19}F MRI sensitivity, consistent with the ^{1}H/^{19}F NMR and FL results.

The responsiveness of fluorinated [5]rotaxanes was further demonstrated through ^{19}F MRI and FLI at a low concentration of 25 μM. First, the incorporation of $\mathbf{W_F}$ into $\mathbf{R'_{5F}}$ and the "wheel-stationing" in $\mathbf{R_{5F}}$ led to an enhancement in ^{19}F MRI SI in the $\mathbf{W_F} \rightarrow \mathbf{R'_{5F}} \rightarrow \mathbf{R_{5F}}$ sequence, attributed to the restricted wheel ^{19}F motion. Simultaneously, FLI SI showed a notable increase in the $\mathbf{A_{TPE}S} \rightarrow \mathbf{R'_{5F}} \rightarrow \mathbf{R_{5F}}$ sequence due to the

G

dramatically restricted TPE motion (Figure 7a). Second, treatment of R_{SF} with sodium hydroxide reduced ^{19}F MRI and FLI SI, while treatment of R'_{SF} with hydrochloric acid increased both signals (Figure 7b). This dual-response "dim-bright" transition, driven by the "stationing-shuttling" motion of the wheels, was reproducible over multiple cycles. In contrast, the treatment of R_{SH} and R'_{SH} with acid or base caused negligible changes in fluorescence emission (Figure 7c).

Next, increasing the water content in R_{SF} solutions enhanced ^{19}F MRI and FLI SI, suggesting that the aggregation-induced restriction of wheel ^{19}F and TPE motions contributed to the observed effects (Figure 7d). Additionally, the shortening of the ^{19}F relaxation time with increasing water content further confirmed the restricted motion of wheel ^{19}F (Figure S18). A pH-responsive FL spectrum study was conducted on R_{SF} in a H_2O-THF (3:7) mixture. As the pH increased from 3.0 to 10.0 by adding sodium hydroxide, a decrease in fluorescence emission was observed (Figures 7e and S19), showing a linear pH-dependent decrease in fluorescence intensity with increased pH. Notably, FLI SI exhibited more dramatic changes than ^{19}F MRI SI (Figure 7a−d), indicating that TPE motion is more sensitive than ^{19}F under the conditions. These findings highlight the sensitivity and responsiveness of fluorinated [5]rotaxanes as dual ^{19}F MRI and FLI agents. However, it is important to note that this pH-responsive fluorescence behavior is not yet suitable for applications in a biological environment. As the primary focus of this study is to demonstrate the feasibility of the mechanical interlocking strategy, we are actively working on improving the water solubility of R_{SF} to extend its potential for future in vivo and biological studies.

Finally, a proof-of-concept study was conducted to investigate the potential of R_{SF} as a dual ^{19}F MRI and FLI agent under physiological conditions. Given its hydrophobic nature and insolubility in water, like most ^{19}F MRI agents, R_{SF} was formulated with clinically used tricaproin into a monodisperse nanoemulsion $R_{SF}NPs$ (particle size: 193 nm, polydispersity index (PDI): 0.166, zeta potential: −38 mV) using lecithin and DSPE-PEG$_{2000}$ as surfactants (Figure 7f). $R_{SF}NPs$ were successfully imaged at a low concentration of 7 μM (C_F = 1 mM) with an SNR of 5.5 (Figures 7g and S20). The relationship between the signal intensity and the ^{19}F concentration followed a linear trend (Figure S20). We then calculated the number of ^{19}F atoms per imaging voxel (^{19}F spins per voxel) to evaluate the detection limit. A threshold SNR of 2.5, consistent with a previous clinical ^{19}F MRI cell tracking study,[55] was applied for this analysis. Under the experimental conditions (a voxel of 17.6 μL and an acquisition time of 768 s), the sensitivity of ^{19}F detection is approximately 0.5 mM (R_{SF} concentration: 3.5 μM), corresponding to a detection limit of ∼5.3 × 10^{15} ^{19}F spins per voxel (Figure S20). This detection limit is lower than those of most reported emulsions containing fluorinated agents[39,56−58] (10^{16}–10^{17} ^{19}F spins per voxel), underscoring the potential of R_{SF} for sensitive ^{19}F MRI. Additionally, the nanoemulsion exhibited strong fluorescence emission (Figure 7g). Following intratumoral injection into U87-MG tumor-bearing BALB/c nude mice, a strong ^{19}F MRI signal was detected (Figure 7h), demonstrating its potential for applications.

CONCLUSIONS

In this study, we demonstrated the development of a single-molecule dual ^{19}F MRI and FLI agent using a [5]rotaxane architecture, overcoming the sensitivity disparity between these two imaging techniques. By integrating fluorinated wheels and a TPE fluorophore into a mechanically interlocked [5]-rotaxane, we achieved enhanced ^{19}F MRI sensitivity at micromolar concentrations and stimulus-responsive fluorescence emission. The ability to modulate the motions of fluorine and fluorophore via "stationing-shuttling" behavior allows for precise control of both imaging modalities, resulting in significant improvements in imaging performance. This work not only bridges the sensitivity gap between ^{19}F MRI and FLI within a single molecule but also introduces a versatile rotaxane strategy for designing high-performance, responsive dual imaging agents. The fluorous effects and steric hindrance in the [5]rotaxane system facilitate uniform wheel motion and enhance responsiveness, underscoring its potential as a high-performance molecular device. This single-molecule dual-modality approach offers promising applications in cancer diagnosis, targeted therapy, and molecular imaging. Ongoing investigations are focused on further enhancing sensitivity and responsiveness, extending the fluorescence wavelength to near-infrared regions, and exploring in vivo applications of fluorinated rotaxanes for multimodal imaging, image-guided drug delivery, and personalized medicine, with results to be reported in subsequent publications.

ASSOCIATED CONTENT

ⓢ Supporting Information

The Supporting Information is available free of charge at https://pubs.acs.org/doi/10.1021/jacs.5c00429.

> Supplementary figures and tables (including ^1H NMR spectra, ^1H−^1H ROESY NMR spectra, ^1H−^{19}F HOESY NMR spectrum, fitting curves for T_1 and T_2, fitting results of F$_W$, H$_o$, and H$_m$, UV absorption spectra, fitted linear relationship, FL emission spectra, maximum FL intensity curves, time-resolution photoluminescence spectra, and normalized FL emission spectra), preparation and characterization of compounds, experimental details, and copies of spectra (PDF)
> Simulated movie of R_{SF} (MP4)
> Simulated movie of R'_{SF} (MP4)
> Simulated movie of R_{SH} (MP4)
> Simulated movie of R'_{SH} (MP4)

AUTHOR INFORMATION

Corresponding Authors

Zhong-Xing Jiang − *School of Pharmaceutical Sciences, Wuhan University, Wuhan 430071, China; State Key Laboratory of Magnetic Resonance Spectroscopy and Imaging, National Center for Magnetic Resonance in Wuhan, Wuhan Institute of Physics and Mathematics, Innovation Academy for Precision Measurement Science and Technology, Chinese Academy of Sciences, Wuhan 430071, China; University of Chinese Academy of Sciences, Beijing 100049, China;* ⓞ orcid.org/0000-0003-2601-4366; Email: zxjiang@apm.ac.cn

Shizhen Chen − *State Key Laboratory of Magnetic Resonance Spectroscopy and Imaging, National Center for Magnetic Resonance in Wuhan, Wuhan Institute of Physics and Mathematics, Innovation Academy for Precision*

Measurement Science and Technology, Chinese Academy of Sciences, Wuhan 430071, China; University of Chinese Academy of Sciences, Beijing 100049, China;
Email: chenshizhen@apm.ac.cn

Authors

Lan Yang − *School of Pharmaceutical Sciences, Wuhan University, Wuhan 430071, China; State Key Laboratory of Magnetic Resonance Spectroscopy and Imaging, National Center for Magnetic Resonance in Wuhan, Wuhan Institute of Physics and Mathematics, Innovation Academy for Precision Measurement Science and Technology, Chinese Academy of Sciences, Wuhan 430071, China*

Fang Wang − *State Key Laboratory of Magnetic Resonance Spectroscopy and Imaging, National Center for Magnetic Resonance in Wuhan, Wuhan Institute of Physics and Mathematics, Innovation Academy for Precision Measurement Science and Technology, Chinese Academy of Sciences, Wuhan 430071, China*

Yu Li − *State Key Laboratory of Magnetic Resonance Spectroscopy and Imaging, National Center for Magnetic Resonance in Wuhan, Wuhan Institute of Physics and Mathematics, Innovation Academy for Precision Measurement Science and Technology, Chinese Academy of Sciences, Wuhan 430071, China*

Rui Zhou − *State Key Laboratory of Magnetic Resonance Spectroscopy and Imaging, National Center for Magnetic Resonance in Wuhan, Wuhan Institute of Physics and Mathematics, Innovation Academy for Precision Measurement Science and Technology, Chinese Academy of Sciences, Wuhan 430071, China*

Anfeng Li − *State Key Laboratory of Magnetic Resonance Spectroscopy and Imaging, National Center for Magnetic Resonance in Wuhan, Wuhan Institute of Physics and Mathematics, Innovation Academy for Precision Measurement Science and Technology, Chinese Academy of Sciences, Wuhan 430071, China*

Tingjuan Wu − *State Key Laboratory of Magnetic Resonance Spectroscopy and Imaging, National Center for Magnetic Resonance in Wuhan, Wuhan Institute of Physics and Mathematics, Innovation Academy for Precision Measurement Science and Technology, Chinese Academy of Sciences, Wuhan 430071, China*

Maosong Qiu − *State Key Laboratory of Magnetic Resonance Spectroscopy and Imaging, National Center for Magnetic Resonance in Wuhan, Wuhan Institute of Physics and Mathematics, Innovation Academy for Precision Measurement Science and Technology, Chinese Academy of Sciences, Wuhan 430071, China*

Lei Zhang − *State Key Laboratory of Magnetic Resonance Spectroscopy and Imaging, National Center for Magnetic Resonance in Wuhan, Wuhan Institute of Physics and Mathematics, Innovation Academy for Precision Measurement Science and Technology, Chinese Academy of Sciences, Wuhan 430071, China*

Minghui Yang − *State Key Laboratory of Magnetic Resonance Spectroscopy and Imaging, National Center for Magnetic Resonance in Wuhan, Wuhan Institute of Physics and Mathematics, Innovation Academy for Precision Measurement Science and Technology, Chinese Academy of Sciences, Wuhan 430071, China;* orcid.org/0000-0003-1067-2217

Xin Zhou − *State Key Laboratory of Magnetic Resonance Spectroscopy and Imaging, National Center for Magnetic Resonance in Wuhan, Wuhan Institute of Physics and Mathematics, Innovation Academy for Precision Measurement Science and Technology, Chinese Academy of Sciences, Wuhan 430071, China; University of Chinese Academy of Sciences, Beijing 100049, China;* orcid.org/0000-0002-5580-7907

Complete contact information is available at:
https://pubs.acs.org/10.1021/jacs.5c00429

REFERENCES

(1) Mizukami, S.; Takikawa, R.; Sugihara, F.; Shirakawa, M.; Kikuchi, K. Dual-Function Probe to Detect Protease Activity for Fluorescence Measurement and ^{19}F MRI. *Angew. Chem., Int. Ed.* **2009**, *48*, 3641−3643.

(2) Wang, Z.; Yue, X.; Wang, Y.; Qian, C.; Huang, P.; Lizak, M.; Niu, G.; Wang, F.; Rong, P.; Kiesewetter, D. O.; Ma, Y.; Chen, X. A Symmetrical Fluorous Dendron-Cyanine Dye-Conjugated Bimodal Nanoprobe for Quantitative ^{19}F MRI and NIR Fluorescence Bioimaging. *Adv. Healthcare Mater.* **2014**, *3*, 1326−1333.

(3) Zhang, Y.; Bo, S.; Feng, T.; Qin, X.; Wan, Y.; Jiang, S.; Li, C.; Lin, J.; Wang, T.; Zhou, X.; Jiang, Z.-X.; Huang, P. A Versatile Theranostic Nanoemulsion for Architecture-Dependent Multimodal Imaging and Dually Augmented Photodynamic Therapy. *Adv. Mater.* **2019**, *31*, No. 1806444.

(4) Zhu, J.; Zhang, H.; Chen, K.; Li, Y.; Yang, Z.; Chen, S.; Zheng, X.; Zhou, X.; Jiang, Z.-X. Peptidic Monodisperse PEG "Comb" as Multifunctional "Add-On" Module for Imaging-Traceable and Thermo-Responsive Theranostics. *Adv. Healthc. Mater.* **2020**, *9*, No. 1901331.

(5) Chen, S.; Xiao, L.; Li, Y.; Qiu, M.; Yuan, Y.; Zhou, R.; Li, C.; Zhang, L.; Jiang, Z.-X.; Liu, M.; Zhou, X. *In Vivo* Nitroreductase Imaging *via* Fluorescence and Chemical Shift Dependent ^{19}F NMR. *Angew. Chem., Int. Ed.* **2022**, *61*, No. e202213495.

(6) Janasik, D.; Krawczyk, T. [19]F MRI Probes for Multimodal Imaging. *Chem.—Eur. J.* **2022**, *28*, No. e202102556.

(7) Li, Y.; Zhang, J.; Zhu, L.; Jiang, M.; Ke, C.; Long, H.; Lin, R.; Ye, C.; Zhou, X.; Jiang, Z.-X.; Chen, S. All-in-One Heptamethine Cyanine Amphiphiles for Dual Imaging-Guided Chemo-Photodynamic-Photothermal Therapy of Breast Cancer. *Adv. Healthc. Mater.* **2023**, *12*, No. 2300941.

(8) Yuan, M.; Han, Z.; Li, Y.; Zhan, X.; Sun, Y.; He, B.; Liang, Y.; Luo, K.; Li, F. A pH-Responsive Nanoplatform with Dual-Modality Imaging for Enhanced Cancer Phototherapy and Diagnosis of Lung Metastasis. *J. Nanobiotechnol.* **2024**, *22*, 180.

(9) Wu, T.; Li, A.; Chen, K.; Peng, X.; Zhang, J.; Jiang, M.; Chen, S.; Zheng, X.; Zhou, X.; Jiang, Z.-X. Perfluoro-*tert*-Butanol: A Corner-

stone for High Performance Fluorine-19 Magnetic Resonance Imaging. *Chem. Commun.* 2021, 57, 7743−7757.

(10) Lee, M. H.; Kim, J. S.; Sessler, J. L. Small Molecule-Based Ratiometric Fluorescence Probes for Cations, Anions, and Biomolecules. *Chem. Soc. Rev.* 2015, 44, 4185−4191.

(11) Tian, X.; Murfin, L. C.; Wu, L.; Lewis, S. E.; James, T. D. Fluorescent Small Organic Probes for Biosensing. *Chem. Sci.* 2021, 12, 3406−3426.

(12) Yue, X.; Taraban, M. B.; Hyland, L. L.; Yu, Y. B. Avoiding Steric Congestion in Dendrimer Growth through Proportionate Branching: A Twist on da Vinci's Rule of Tree Branching. *J. Org. Chem.* 2012, 77, 8879−8887.

(13) Yu, Y. B. Fluorinated Dendrimers as Imaging Agents for ^{19}F MRI. *WIREs Nanomed. Nanobiotechnol.* 2013, 5, 646−661.

(14) Yu, W.; Yang, Y.; Bo, S.; Li, Y.; Chen, S.; Yang, Z.; Zheng, X.; Jiang, Z.-X.; Zhou, X. Design and Synthesis of Fluorinated Dendrimers for Sensitive ^{19}F MRI. *J. Org. Chem.* 2015, 80, 4443−4449.

(15) Janjic, J. M.; Srinivas, M.; Kadayakkara, D. K. K.; Ahrens, E. T. Self-Delivering Nanoemulsions for Dual Fluorine-19 MRI and Fluorescence Detection. *J. Am. Chem. Soc.* 2008, 130, 2832−2841.

(16) Tirotta, I.; Dichiarante, V.; Pigliacelli, C.; Cavallo, G.; Terraneo, G.; Bombelli, F. B.; Metrangolo, P.; Resnati, G. [19]F Magnetic Resonance Imaging (MRI): From Design of Materials to Clinical Applications. *Chem. Rev.* 2015, 115, 1106−1129.

(17) Li, Y.; Zhang, H.; Guo, C.; Hu, G.; Wang, L. Multiresponsive Nanoprobes for Turn-On Fluorescence/^{19}F MRI Dual-Modal Imaging. *Anal. Chem.* 2020, 92, 11739−11746.

(18) Zhang, C.; Yan, K.; Fu, C.; Peng, H.; Hawker, C. J.; Whittaker, A. K. Biological Utility of Fluorinated Compounds: from Materials Design to Molecular Imaging, Therapeutics and Environmental Remediation. *Chem. Soc. Rev.* 2022, 122, 167−208.

(19) Xie, D.; Yu, M.; Kadakia, R. T.; Que, E. L. [19]F Magnetic Resonance Activity-Based Sensing Using Paramagnetic Metals. *Acc. Chem. Res.* 2020, 53, 2−10.

(20) Mo, Y.; Huang, C.; Liu, C.; Duan, Z.; Liu, J.; Wu, D. Recent Research Progress of [19]F Magnetic Resonance Imaging Probes: Principle, Design, and Their Application. *Macromol. Rapid Commun.* 2023, 44, No. 2200744.

(21) Zhao, Z.; Lam, J. W. Y.; Tang, B. Z. Tetraphenylethene: A Versatile AIE Building Block for the Construction of Efficient Luminescent Materials for Organic Light-Emitting Diodes. *J. Mater. Chem. B* 2012, 22, 23726−23740.

(22) Kumar, K. S. S.; Girish, Y. R.; Ashrafizadeh, M.; Mirzaei, S.; Rakesh, K. P.; Gholami, M. H.; Zabolian, A.; Hushmandi, K.; Orive, G.; Kadumudi, F. B.; Dolatshahi-Pirouz, A.; Thakur, V. K.; Zarrabi, A.; Makvandi, P.; Rangappa, K. S. AIE-featured Tetraphenylethylene Nanoarchitectures in Biomedical Application: Bioimaging, Drug Delivery and Disease Treatment. *Coord. Chem. Rev.* 2021, 447, 214135−214182.

(23) Mei, J.; Hong, Y.; Lam, J. W.; Qin, A.; Tang, Y.; Tang, B. Z. Aggregation-Induced Emission: The Whole is More Brilliant than the Parts. *Adv. Mater.* 2014, 26, 5429−5479.

(24) Mei, J.; Leung, N. L. C.; Kwok, R. T. K.; Lam, J. W. Y.; Tang, B. Z. Aggregation-Induced Emission: Together We Shine, United We Soar! *Chem. Soc. Rev.* 2015, 115, 11718−11940.

(25) Asthana, S.; Mouli, M.; Tamrakar, A.; Wani, M. A.; Mishra, A. K.; Pandey, R.; Pandey, M. D. Recent Advances in AIEgen-based Chemosensors for Small Molecule Detection, with A Focus on Ion Sensing. *Anal. Methods* 2024, 16, 4431.

(26) Kislukhin, A. A.; Xu, H.; Adams, S. R.; Narsinh, K. H.; Tsien, R. Y.; Ahrens, E. T. Paramagnetic Fluorinated Nanoemulsions for Sensitive Cellular Fluorine-19 Magnetic Resonance Imaging. *Nat. Mater.* 2016, 15, 662−668.

(27) Lin, H.; Tang, X.; Li, A.; Gao, J. Activatable ^{19}F MRI Nanoprobes for Visualization of Biological Targets in Living Subjects. *Adv. Mater.* 2021, 33, No. e2005657.

(28) Li, A.; Luo, X.; Chen, D.; Li, L.; Lin, H.; Gao, J. Small Molecule Probes for [19]F Magnetic Resonance Imaging. *Anal. Chem.* 2023, 95, 70−82.

(29) Cai, X.; Liu, B. Aggregation-Induced Emission: Recent Advances in Materials and Biomedical Applications. *Angew. Chem., Int. Ed.* 2020, 59, 9868−9886.

(30) Zhu, X.; Zhang, P.; Liu, D.; Tao, L.; Du, J.; Gao, X. Stimuli-Responsive ^{19}F MRI Probes: From Materials Design to *in vitro* Detection and *in Vivo* Diagnosis. *Trends Anal. Chem.* 2024, 172, No. 117607.

(31) Sauvage, J. P. From Chemical Topology to Molecular Machines (Nobel Lecture). *Angew. Chem., Int. Ed.* 2017, 56, 11080−11093.

(32) Stoddart, J. F. Mechanically Interlocked Molecules (MIMs)-Molecular Shuttles, Switches, and Machines (Nobel Lecture). *Angew. Chem., Int. Ed.* 2017, 56, 11094−11125.

(33) Amano, S.; Fielden, S. D. P.; Leigh, D. A. A Catalysis-Driven Artificial Molecular Pump. *Nature* 2021, 594, 529−534.

(34) Feng, Y.; Ovalle, M.; Seale, J. S. W.; Lee, C. K.; Kim, D. J.; Astumian, R. D.; Stoddart, J. F. Molecular Pumps and Motors. *J. Am. Chem. Soc.* 2021, 143, 5569−5591.

(35) Binks, L.; Tian, C.; Fielden, S. D. P.; Vitorica-Yrezabal, I. J.; Leigh, D. A. Transamidation-Driven Molecular Pumps. *J. Am. Chem. Soc.* 2022, 144, 15838−15844.

(36) Chen, L.; Sheng, X.; Li, G.; Huang, F. Mechanically Interlocked Polymers Based on Rotaxanes. *Chem. Soc. Rev.* 2022, 51, 7046−7065.

(37) Binks, L.; Borsley, S.; Gingrich, T. R.; Leigh, D. A.; Penocchio, E.; Roberts, B. M. W. The Role of Kinetic Asymmetry and Power Strokes in An Information Ratchet. *Chem.* 2023, 9, 2902−2917.

(38) Yang, L.; Li, Y.; Jiang, M.; Zhou, R.; Cong, H.; Yang, M.; Zhang, L.; Li, S.; Yang, Y.; Liu, M.; Zhou, X.; Jiang, Z.-X.; Chen, S. Fluorinated [2]Rotaxanes as Sensitive ^{19}F MRI Agents: Threading for Higher Sensitivity. *Chin. Chem. Lett.* 2024, 35, No. 109512.

(39) Tirotta, I.; Mastropietro, A.; Cordiglieri, C.; Gazzera, L.; Baggi, F.; Baselli, G.; Bruzzone, M. G.; Zucca, I.; Cavallo, G.; Terraneo, G.; Bombelli, F. B.; Metrangolo, P.; Resnati, G. A Superfluorinated Molecular Probe for Highly Sensitive *in Vivo* ^{19}F-MRI. *J. Am. Chem. Soc.* 2014, 136, 8524−8527.

(40) Rosati, M.; Acocella, A.; Pizzi, A.; Turtù, G.; Neri, G.; Demitri, N.; Nonappa; Raffaini, G.; Donnio, B.; Zerbetto, F.; Bombelli, F. B.; Cavallo, G.; Metrangolo, P. Janus-Type Dendrimers Based on Highly Branched Fluorinated Chains with Tunable Self-Assembly and [19]F Nuclear Magnetic Resonance Properties. *Macromolecules* 2022, 55, 2486−2496.

(41) Bona, B. L.; Koshkina, O.; Chirizzi, C.; Dichiarante, V.; Metrangolo, P.; Bombelli, F. B. Multibranched-Based Fluorinated Materials: Tailor-Made Design of ^{19}F-MRI Probes. *Acc. Mater. Res.* 2023, 4, 71−85.

(42) Sancho-Albero, M.; Ayaz, N.; Sebastian, V.; Chirizzi, C.; Encinas-Gimenez, M.; Neri, G.; Chaabane, L.; Luján, L.; Martin-Duque, P.; Metrangolo, P.; Santamaría, J.; Bombelli, F. B. Super-fluorinated Extracellular Vesicles for *In Vivo* Imaging by ^{19}F-MRI. *ACS Appl. Mater. Interfaces* 2023, 15, 8974−8985.

(43) Zhang, Z.-J.; Zhang, H.-Y.; Wang, H.; Liu, Y. A Twin-Axial Hetero[7]Rotaxane. *Angew. Chem., Int. Ed.* 2011, 50, 10834−10838.

(44) Rao, S.-J.; Zhang, Q.; Mei, J.; Ye, X.-H.; Gao, C.; Wang, Q.-C.; Qu, D.-H.; Tian, H. One-pot Synthesis of Hetero[6]rotaxane Bearing Three Different Kinds of Acrocycle Through A Self-Sorting Process. *Chem. Sci.* 2017, 8, 6777−6783.

(45) Groppi, J.; Casimiro, L.; Canton, M.; Corra, S.; Jafari-Nasab, M.; Tabacchi, G.; Cavallo, L.; Baroncini, M.; Silvi, S.; Fois, E.; Credi, A. Precision Molecular Threading/Dethreading. *Angew. Chem., Int. Ed.* 2020, 59, 14825−14834.

(46) Krafft, M. P. Applications of Fluorous Compounds in Materials Chemistry: Basic Principles and Recent Advances in Fluorinated Self-Assemblies and Colloidal Systems. In *Handbook of Fluorous Chemistry*, Gladysz, J. A.; Curran, D. P.; Horvath, I. T., Eds.; WILEY-VCH: Weinheim, Germany, 2004; 478−490.

J

(47) Cametti, M.; Crousse, B.; Metrangolo, P.; Milani, R.; Resnati, G. The Fluorous Effect in Biomolecular Applications. *Chem. Soc. Rev.* **2012**, *41*, 31−42.

(48) Blanco, V.; Carlone, A.; Hanni, K. D.; Leigh, D. A.; Lewandowski, B. A Rotaxane-Based Switchable Organocatalyst. *Angew. Chem., Int. Ed.* **2012**, *51*, 5166−5169.

(49) Curcio, M.; Nicoli, F.; Paltrinieri, E.; Fois, E.; Tabacchi, G.; Cavallo, L.; Silvi, S.; Baroncini, M.; Credi, A. Chemically Induced Mismatch of Rings and Stations in [3]Rotaxanes. *J. Am. Chem. Soc.* **2021**, *143*, 8046−8055.

(50) Bain, A. D. Chemical Exchange in NMR. *Prog. Nucl. Magn. Reson. Spectrosc.* **2003**, *43*, 63−103.

(51) Xu, X.-Q.; Wang, X.-Q.; Wang, W. Lighting up Rotaxanes with AIEgens. *Chin. Chem. Lett.* **2023**, *34*, 107665.

(52) Dong, S.; Xu, G.; Hoffmann, H. Aggregation Behavior of Fluorocarbon and Hydrocarbon Cationic Surfactant Mixtures: A Study of ^{1}H NMR and ^{19}F NMR. *J. Phys. Chem. B* **2008**, *112*, 9371−9378.

(53) Wang, X.; Chen, J.; Wang, D.; Dong, S.; Hao, J.; Hoffmann, H. Monitoring the Different Micelle Species and the Slow Kinetics of Tetraethylammonium Perfluorooctane-Sulfonate by ^{19}F NMR Spectroscopy. *Adv. Colloid Interface Sci.* **2017**, *246*, 153−164.

(54) Cai, L.; Chen, Q.; Guo, J.; Liang, Z.; Fu, D.; Meng, L.; Zeng, J.; Wan, Q. Recyclable Fluorous-Tag Assisted Two-Directional Oligosaccharide Synthesis Enabled by Interrupted Pummerer Reaction Mediated Glycosylation. *Chem. Sci.* **2022**, *13*, 8759−8765.

(55) Ahrens, E. T.; Helfer, B. M.; O'Hanlon, C. F.; Schirda, C. Clinical Cell Therapy Imaging Using a Perfluorocarbon Tracer and Fluorine-19 MRI. *Magn. Reson. Med.* **2014**, *72*, 1696−1701.

(56) Mastropietro, A.; De Bernardi, E.; Breschi, G. L.; Zucca, I.; Cametti, M.; Soffientini, C. D.; de Curtis, M.; Terraneo, G.; Metrangolo, P.; Spreafico, R.; Resnati, G.; Baselli, G. Optimization of Rapid Acquisition with Relaxation Enhancement (RARE) Pulse Sequence Parameters for ^{19}F-MRI Studies. *Magn. Reson. Imaging* **2014**, *40*, 162−170.

(57) Heaton, A. R.; Lechuga, L. M.; Tangsangasaksri, M.; Ludwig, K. D.; Fain, S. B.; Mecozzi, S. A Stable, Highly Concentrated Fluorous Nanoemulsion Formulation for *in Vivo* Cancer Imaging *via* ^{19}F-MRI. *NMR Biomed.* **2024**, *37*, No. e5100.

(58) Chen, J.; Pal, P.; Ahrens, E. T. Systems Engineering Approach Towards Sensitive Cellular Fluorine-19 MRI. *NMR Biomed.* **2025**, *38*, No. e5298.